Biochemistry

pubs.acs.org/biochemistry Article

p53 Is Potentially Regulated by Cyclophilin D in the Triple-Proline Loop of the DNA Binding Domain

Jacques Kumutima, Xin-Qiu Yao, and Donald Hamelberg*

Cite This: *Biochemistry* 2021, 60, 597−606 Read Online

ACCESS | Metrics & More | Article Recommendations | Supporting Information

ABSTRACT: The multifunctional protein p53 is the central molecular sensor of cellular stresses. The canonical function of p53 is to transcriptionally activate target genes in response to, for example, DNA damage that may trigger apoptosis. Recently, p53 was also found to play a role in the regulation of necrosis, another type of cell death featured by the mitochondrial permeability transition (mPT). In this process, p53 directly interacts with the mPT regulator cyclophilin D, the detailed mechanism of which however remains poorly understood. Here, we report a comprehensive computational investigation of the p53−cyclophilin D interaction using molecular dynamics simulations and associated analyses. We have identified the specific cyclophilin D binding site on p53 that is located at proline 151 in the DNA binding domain. As a peptidyl-prolyl isomerase, cyclophilin D binds p53 and catalyzes the *cis*−*trans* isomerization of the peptide bond preceding proline 151. We have also characterized the effect of such an isomerization and found that the p53 domain in the *cis* state is overall more rigid than the *trans* state except for the local region around proline 151. Dynamical changes upon isomerization occur in both local and distal regions, indicating an allosteric effect elicited by the isomerization. We present potential allosteric communication pathways between proline 151 and distal sites, including the DNA binding surface. Our work provides, for the first time, a model for how cyclophilin D binds p53 and regulates its activity by switching the configuration of a specific site.

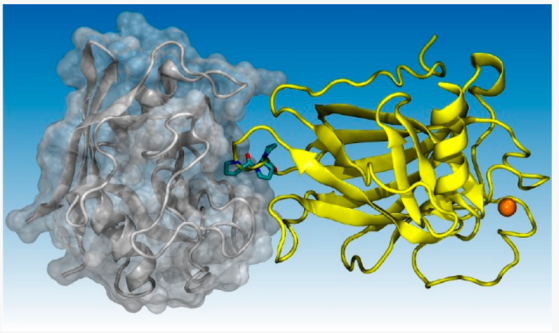

The tumor suppressor p53 is an essential protein that regulates cell division and growth.[1] Known as the guardian of the genome, p53 responds to the damage of DNA by activating or repressing the transcription of target genes that lead to cell cycle arrest and DNA repair, or triggering programmed cell death (apoptosis) if the damage is unrepairable. Entire human p53 functions as a homotetramer,[2] with each monomer composed of 393 residues forming four domains of distinct functions: the N-terminal transcriptional activation domain, the DNA binding domain (DBD), the tetramerization domain, and the C-terminal regulatory domain.[3] Each p53 DBD of the tetramer, consisting of residues 94−292 and displaying an overall β-sandwich structure (Figure 1A), works as a separate domain and is the central component of the protein responsible for binding specific DNA sequences. More than 50% of human tumors are associated with mutations in p53, most of which occur in p53 DBD whose phenotypes include protein misfolding and misregulation of protein expression.[4,5] Recently, p53 has also been found to interact with various mitochondrial targets that mediate the mitochondrial permeability transition (mPT).[6] The mPT-regulatory activity of p53 in cells is a response to oxidative stress, which ultimately leads to necrosis, a premature cell death that is usually caused by injury-induced autolysis.[6,7] On one side, necrosis is good because it can kill cancer cells.[8] On the other side, however, necrosis can cause ischemia or reperfusion in cerebral stroke and myocardial infarction.[9]

An important mPT regulator is cyclophilin D (CypD). Cyclophilins are peptidyl-prolyl isomerases that catalyze the *cis*−*trans* interconversion of the peptide bond preceding a proline.[10] Cyclophilins have various functions, including the regulation of protein folding/unfolding processes and immune responses.[11,12] There are 17 isoforms of human cyclophilins.[13] CypD is the only cyclophilin isoform located in the mitochondria,[10] and its activity can be suppressed by the cyclophilin inhibitor, cyclosporin.[14,15] CypD interacts with multiple protein targets such as adenine nucleotide translocase, α-peroxisome proliferator-activated receptor, and α-synuclein[16] and regulates various cellular processes, including the exchange of calcium through the opening of the mPT pore,[17] various forms of cellular necrotic death,[18,19] and apoptosis.[15,20] CypD inhibits senescence, and CypD deletion suppresses *in vivo* Ras tumorigenesis.[21] CypD-mediated mPT dysfunction is

Received: December 7, 2020
Revised: January 5, 2021
Published: February 16, 2021

https://dx.doi.org/10.1021/acs.biochem.0c00946
Biochemistry 2021, 60, 597−606

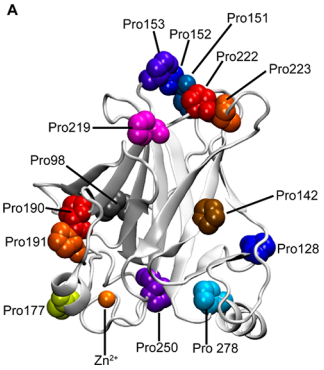

B

Simulation ID	Substrates
Pro98	Ace-S-S-S-V-**P**-S-Q-K-T-Y-Nme
Pro128	Ace-C-T-Y-S-**P**-A-L-N-K-M-Nme
Pro142	Ace-A-K-T-C-**P**-V-Q-L-W-V-Nme
Pro151	Ace-V-D-S-T-**P**-P-P-G-T-R-Nme
Pro152	Ace-D-S-T-P-**P**-P-G-T-R-V-Nme
Pro153	Ace-S-T-P-P-**P**-G-T-R-V-R-Nme
Pro177	Ace-V-R-R-C-**P**-H-H-E-R-C-Nme
Pro190	Ace-D-G-L-A-**P**-P-Q-H-L-I-Nme
Pro191	Ace-G-L-A-P-**P**-Q-H-L-I-R-Nme
Pro219	Ace-S-V-V-V-**P**-Y-E-P-P-E-Nme
Pro222	Ace-V-P-Y-E-**P**-P-E-V-G-S-Nme
Pro223	Ace-P-Y-E-P-**P**-E-V-G-S-D-Nme
Pro250	Ace-M-N-R-R-**P**-I-L-T-I-I-Nme
Pro278	Ace-V-C-A-C-**P**-G-R-D-R-R-Nme

Figure 1. Multiple potential CypD binding sites on p53. (A) The DNA binding domain of p53 (Protein Data Bank entry 1TUP) is represented by a white cartoon, where all prolines are shown as van der Waals spheres in different colors. The zinc ion (Zn^{2+}) is represented by an orange sphere. (B) List of simulations testing the peptidyl-prolyl *cis*−*trans* isomerization at different proline sites of p53 by CypD. Substrate sequences, with residues forming the tested prolyl peptide bond highlighted in bold, are derived from p53. All sequences are 10 amino acids long and capped at the N- and C-termini with acetyl and *N*-methylamide, respectively.

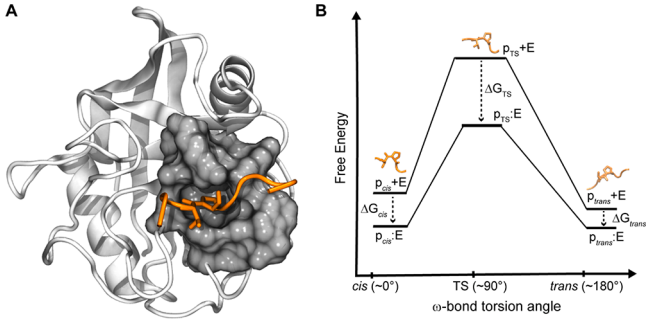

Figure 2. Peptidyl-prolyl *cis*−*trans* isomerization in CypD. (A) Model of CypD (white cartoon; Protein Data Bank entry 4O8H) interacting with a p53 truncated peptide (orange). The peptide binds in the active-site pocket (gray surface) of CypD. (B) Schematic free energy profiles of the *cis*-TS (transition state)−*trans* conversion pathway during the isomerization of the peptide in a free solution (indicated by a plus sign, e.g., p_{cis}+E) and in CypD (indicated by a colon, e.g., p_{cis}:E). The enzyme can catalyze both directions of *cis* to *trans* and *trans* to *cis*. The larger free energy reduction at TS indicates that the enzyme binds a peptide in the transition state better than in the ground state (*cis* or *trans*).

linked to various diseases, including Alzheimer's disease and Parkinson's disease.[22,23] Hence, CypD is an important therapeutic drug target.[14]

Cyclophilin D is the major component of the mPT pore complex that interacts with p53. Evidence has shown that CypD mainly binds to p53 DBD and catalyzes the prolyl isomerization in the domain,[6,24] which may lead to p53 aggregation.[25] The p53 DBD has 14 proline sites surrounded with various amino acid sequences (Figure 1A,B), all of which could potentially be the CypD binding site. Although both experiment and computational modeling have revealed that p53 binds to the catalytic site of CypD,[25,26] the specific site of interaction on the p53 side remains elusive. So far, how exactly CypD and p53 interact remains poorly understood. Understanding the mechanism of CypD−p53 complexation is pharmaceutically significant. The CypD−p53 complex has been demonstrated to cause cell necroptotic death,[6] a potential anticancer therapeutic pathyway.[8] It has also been determined that CypD activity in breast epithelial cells is p53-dependent and the disruption of CypD−p53 interaction has led to a decrease in the number of tumor cells.[21] Thus, interaction of CypD with p53 has impactful tumorigenic activity. The immunosuppressant cyclosporin A (CsA) prevents formation of the CypD−p53 complex and thus has anticancer efficacy.[6] Small peptide CypD inhibitors that mimic the action of CsA but have improved specificity, solubility, and bioavailability[27−29] could be more potent drug candidates.

In this work, we investigate the mechanism of CypD−p53 interaction and predict the CypD binding site on the p53 DBD using molecular dynamics (MD) simulations and free energy calculations. We have scanned all 14 proline sites by analyzing the thermodynamic properties of the interaction between CypD and peptides derived from the p53 DBD (Figure 1B). Specifically, we have calculated binding free energies between CypD and the p53 peptides in distinct conformational states (*cis*, transition state or TS, and *trans*) along the *cis*−*trans* isomerization, which can be used to depict changes in the free energy profile of the reaction in the absence and presence of the enzyme (Figure 2). To reduce the size of systems, the p53 peptides were truncated to be 10 amino acids in length, with the targeted proline in the middle of the peptide sequence and spatially placed in the active site of CypD. We assume that the CypD binding site is where the peptidyl-prolyl isomerization can be catalyzed efficiently for both *cis*-to-*trans* and *trans*-to-*cis* directions. The efficiency of catalysis is determined by two factors: (1) reduction of the energetic barrier for isomerization upon binding to the enzyme and (2) binding affinity of the substrate in ground states (*cis* and *trans*). The decrease in the energy barrier is the primary requirement for CypD to catalyze isomerization, which can be calculated by the relative binding free energy between a substrate in TS and the same substrate in a ground state. A large barrier reduction indicates a substantial stabilization of the activation complex with respect to ground states by the enzyme.[30,31] A certain amount of ground-state binding affinity is also required for the catalysis to occur efficiently, because otherwise only a tiny fraction of enzymes are occupied at each time. Using this approach, we have identified the triple-proline loop, especially proline 151, to be the most promising binding site for CypD, which is in the loop >30 Å from the DNA binding site and containing three consecutive prolines (Pro151−Pro153). We have also examined the allosteric effect of the isomerization at Pro151, showing how CypD binding and catalysis can potentially modulate both local and distal structural dynamics of the p53 DBD, including the DNA binding surface.

COMPUTATIONAL METHODS

System Preparation. Atomic coordinates of CypD and the p53 DNA binding domain were obtained from the crystallographic structures of Protein Data Bank (PDB) entries 4O8H and 1TUP,[32,33] respectively. CypD−p53 peptide complexes were modeled as previously described.[34] Briefly, initial coordinates of the peptide substrate in the *cis* conformation were taken directly from the previous simulation study. Amino acid names were modified to match the 10-residue truncated p53 peptides (with the targeted proline located at position 5) shown in Figure 1B. Side-chain atoms were removed and then added back for the new peptide using the tLEaP program of AMBER 16.[35] All peptide sequences

https://dx.doi.org/10.1021/acs.biochem.0c00946
Biochemistry 2021, 60, 597−606

were capped with acetyl (ACE) at the N-terminus and *N*-methylamide (NME) at the C-terminus using tLEaP. In total, 14 CypD−p53 (*cis*) complex models were constructed. To prepare other conformations, we performed a series of short (1 ns) restrained MD to rotate the Xaa-Pro peptide bond dihedral angle from *cis* to TS and then to *trans*, with Xaa being the residue preceding the targeted proline. The dihedral angle was defined by C_α and O atoms from Xaa and C_δ and C_α atoms from the proline. The angle for the transition state was assumed to be ∼90°, which is supported by our previous studies.[30,36−39] The angle was rotated with a 10° increment, from 0° (*cis*) to 90° (TS) and then from 90° to 180° (*trans*). The force constant (k = 200 kcal mol^{-1} rad^{-2}) was used to restrain the angle around each reference value. The final structures of the corresponding restrained MD were used as the starting points of longer production MD runs for TS and *trans*, where the targeted dihedral angle was visually inspected and validated with VMD.[40] The MD simulations in the preparation (equilibration) step were performed under the same conditions as those in production (see below). To demonstrate how CypD and p53 interact, the complex of CypD and the entire p53 DBD was also prepared by structurally superimposing the identified CypD binding site (the triple-proline loop) onto the peptide in the CypD−Pro151 complex. In the model, proline 151 is placed in the active site of CypD and shown in the *trans* conformation.

Molecular Dynamics Simulation. We used the AMBER 16 suite of programs and the modified version of AMBER ff14SB force field parameters.[41] Reoptimized parameters for the backbone ω torsion angle were employed.[42] The protonation state of ionizable residues was determined on the basis of pK_a value at pH 7.0 calculated with PROPKA 3.1.[43] The tautomer state of the imidazole side chain of neutral histidine residues was determined by visual inspection of the local structural environment of the residues with PyMOL (Schrödinger, LLC). The protonation and tautomer states of all histidine residues are listed in Table S1. The systems were solvated in a periodic octahedral box filled with pre-equilibrated TIP3P water molecules.[44,45] The box faces were at least 10 Å apart from the system. Original water molecules from the crystallographic structures were kept. The systems were then neutralized by counterions (Na^+ or Cl^- ions). The systems were subjected to 5000 steps of energy minimization (3000 steps of steepest descent and 2000 steps of conjugate gradient). During energy minimization, the positions of the solute atoms were held by harmonic restraints. Five rounds of energy minimization were performed, where the force constant of the positional restraint was gradually reduced from 500 kcal mol^{-1} Å^{-2} to 0. Heating was performed from 100 to 300 K (Langevin thermostat with a collision frequency γ of 1.0 ps^{-1}) within 500 ps under *NVT* conditions with a 1 fs time step and positional restraints to the solute. Five rounds of heating were performed, where the force constant of restraint was set to 500, 300, 100, 50, and 5 kcal mol^{-1} Å^{-2}. A 1 ns equilibration was performed with a 2 fs time step and no restraint under *NPT* conditions (300 K and 1 bar; Monte Carlo barostat with a coupling constant τ_p of 1.0 ps). Each production simulation was performed for a period of ∼1.2 μs (for CypD−p53 peptide complexes; the slight variation of simulation time depended on whether the system was well equilibrated as measured by the backbone root-mean-square deviation) or 500 ns (for p53 DBD-only systems and the CypD−p53 DBD complex) under the same conditions of equilibration. For the CypD−p53 peptide (TS), a dihedral restraint was imposed to keep the unstable 90° peptidyl-prolyl torsion angle, with a k of 200 kcal mol^{-1} rad^{-2}. Particle mesh Ewald (PME) summation was used to evaluate long-range electrostatic interactions.[46] A cutoff of 9 Å was applied for short-range nonbonded interactions. All bonds involving hydrogen atoms in the solute were constrained with the SHAKE[47] algorithm. A simulation snapshot was saved every 1 ps.

Binding Free Energy and Solvent-Accessible Surface Area Calculation. Binding free energies were calculated using the molecular mechanics/Poisson−Boltzmann surface area (MM/PBSA) approach[48] implemented in AMBER16. The SANDER[35] program of AMBER16 was used to compute the gas-phase and solvation terms of binding free energy between CypD and the peptides. The binding energy was calculated for 1% of the total simulation frames. The dielectric constants were set to 1.0 and 80.0 for the interior and exterior of the proteins, respectively. Statistics of energies were computed with the ggplot2 R package.[49] The error estimate was made by splitting each trajectory into five chunks of equal lengths. Then, the mean binding free energy was calculated for each chunk, and the standard error of the mean was defined by SD/$\sqrt{N}$, where SD is the standard deviation of the mean and N = 5 is the number of chunks. Solvent-accessible surface areas were calculated using the CPPTRAJ program[50] of AMBER 16 taking the initial structure of the p53 DBD (*trans*) simulation as the input.

Principal Component Analysis and Root-Mean-Square Fluctuation. PCA was performed using the CPPTRAJ program[50] of AMBER 16 on trajectories derived from MD simulations. Structural superimposition was performed on the basis of backbone atoms (N, Cα, C, and O) for all of the conformational snapshots. Eigenvalues and eigenvectors were calculated from the variance−covariance matrix characterizing the internal motions. Each eigenvector represents a principal component (PC), and the associated eigenvalue describes the structural variance captured by the PC. The first two PCs capturing the largest structural variance (PC1 and PC2) were used to build the subspace where simulation trajectories were projected (the so-called conformer plot) for the subsequent interconformer relationship analysis. Plots of PC1−PC2 projections were generated by ggplot2,[49] and molecular structures were rendered by VMD.[40] To measure the flexibility of residues, the residue-wise averaged atomic root-mean-square fluctuation (RMSF) was calculated using CPPTRAJ and the results were analyzed with the Bio3D R package.[51,52] Prior to the calculation, structures were superimposed on the basis of backbone atoms. The differential RMSF (ΔRMSF) was calculated by subtracting the RMSF of a residue in one simulation from that of the same residue in the other simulation, and the values were mapped onto a molecular structure rendered by PyMOL (Schrödinger, LLC).

Residue−Residue Contact Analysis. Residue contact analysis was performed to understand conformational changes observed in MD simulations. The contact analysis was done following the method previously developed.[53,54] A contact is formed if the minimal non-hydrogen atomic distance between two residues is at most 4.5 Å apart,[54−56] and the residues are separated by at least three amino acids in sequence (i.e., i to $i + n$, where $n \geq 3$). The residue contact was examined for each simulation frame, and the probability of the occurrence of each contact was calculated over the trajectory. Then, contact probability changes from one simulation to the other were

https://dx.doi.org/10.1021/acs.biochem.0c00946
Biochemistry 2021, 60, 597−606

calculated to measure the residue-wise conformational change. While PCA mainly describes the backbone dynamics, contact analysis captures the dynamics of both the backbone and side chains and so is more sensitive. The contact probability changes were further dissected by a residue community analysis using the difference contact network analysis (dCNA) method.[57] The dCNA community analysis provides a simpler representation of the residue contact changes, which can help identify significant conformational changes and provide insights into the allosteric communication between distal protein regions. The contact analysis was performed via Bio3D[51,52] and in-house scripts.

RESULTS AND DISCUSSION

Proline 151 Is the Potential Binding Site of CypD on the p53 DNA Binding Domain. We have compared the free energy profiles of *cis*−*trans* isomerization in a free solution and in CypD for all 14 proline sites (including two diproline sites and one triproline site) of the p53 DBD (see Figure 1B for sequences used as CypD substrates), using MD simulations. As explained by Figure 2B, if a substrate in the transition state or TS shows a binding free energy (ΔG) that is lower than those in the ground states, the energy barrier for the reaction to proceed is reduced; in other words, the isomerization of the substrate can be catalyzed by CypD. We assumed that the CypD binding site on p53 is that near a catalyzable peptidyl-prolyl bond. By examining the binding free energies of each substrate sequence in *cis*, TS, and *trans* conformations, we identified eight Xaa-Pro bonds on the p53 DBD (Pro98, Pro128, Pro142, Pro151, Pro152, Pro153, Pro191, and Pro278) that can potentially be catalyzed by CypD. Examples of binding energy distributions of catalyzable and non-catalyzable bonds are shown in Figure 3, and the results of all Xaa-Pro bonds are given in the Supporting Information.

For all eight identified catalyzable Xaa-Pro bonds, the transition state is significantly stabilized compared to ground states upon binding to CypD (see Figure 4 and Table S2). For example, the mean binding free energy difference ($\Delta\Delta G$) between the TS and ground states for proline 151 (Figure 3A) is −10.79 kcal/mol for *cis* and −13.59 kcal/mol for *trans*. Similarly, for proline 278 (Figure 3B), the values are −6.81 kcal/mol for *cis* and −22.74 kcal/mol for *trans*. The stabilization of the transition state is a common phenomenon in catalysis of many enzymes, including peptidyl-prolyl isomerases.[30] The magnitude of TS thermal stabilization is equivalent to the reduction of the energy barrier that determines whether the catalysis can take place [we note that for the catalysis to occur efficiently, absolute binding free energies of the ground states also matter, which have to be negative or near zero (see below for more discussion)]. In contrast, for noncatalyzable bonds, the stability of TS is either unaltered or reduced compared to that of at least one ground state (Figure 4 and Table S2). For example, the mean binding free energy difference between the TS and either ground state preceding proline 222 is positive (Figure 3C). For proline 250 (Figure 3D), the TS is destabilized especially compared to the *trans* state ($\Delta\Delta G$ = 5.66 kcal/mol).

Among proline sites associated with the eight catalyzable prolyl bonds, Pro151 is shown to be the most promising site for CypD binding. We assume that the CypD binding site is where the nearby peptidyl-prolyl isomerization can be catalyzed by the enzyme with high efficiency for both *cis*-to-*trans* and *trans*-to-*cis* directions. The efficiency of catalysis is

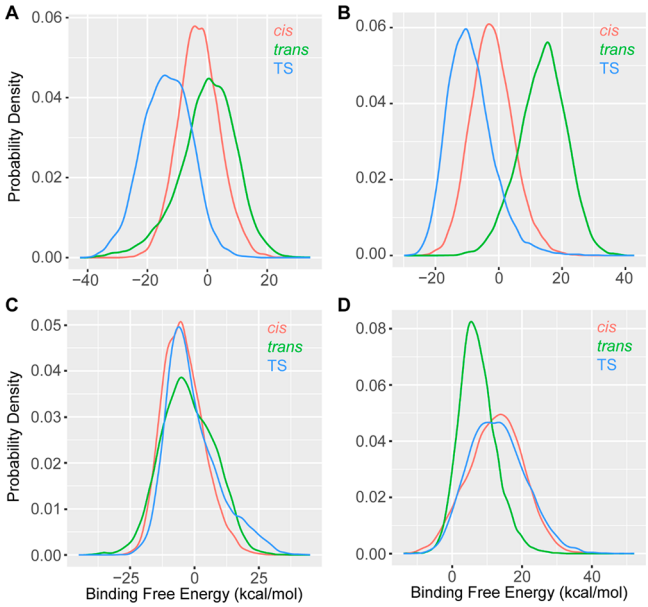

Figure 3. Example probability distributions of the binding free energy between CypD and p53 peptides. Panels A (Pro151) and B (Pro278) show the results for peptides where the peptidyl-prolyl isomerization is predicted to be catalyzed by CypD. Both panels show an apparent shift of binding free energy for the peptide in the transition state (TS) toward more negative values compared to those in ground states, suggesting a reduction of the energy barrier in both peptides. The corresponding prolines represent potential CypD binding sites on the DNA binding domain of p53. In contrast, for peptides in panels C (Pro222) and D (Pro250), catalysis is unlikely to occur because the TS binding free energy is either no different from those of ground states (suggesting that the energy barrier of isomerization remains as high as that of the free peptide) or positive (indicating an inhibitory rather than a catalytic effect). The full set of binding free energy distributions of all tested peptides is provided in the Supporting Information.

determined by not only the magnitude of activation energy reduction (i.e., the relative binding free energy between the TS and ground states, $\Delta\Delta G$) but also the ground-state binding affinity (ΔG_{cis} or ΔG_{trans}). For all of the catalyzable bonds, $\Delta\Delta G$ is always negative, indicating that isomerization reactions are largely accelerated once the substrate is bound in the enzyme. Intriguingly, for all of those bonds the transition from *trans* to *cis* has a more negative $\Delta\Delta G$, suggesting that the corresponding direction of catalysis is preferred within the enzyme (Figure 4). However, for many of those bonds, the binding free energy for the *trans* form is highly positive (see Table S2), suggesting that the largely accelerated *trans*-to-*cis* isomerization (if it occurs) is mainly due to the creation of a disfavored environment for the ground state in the enzyme. Positive ΔG_{trans} values indicate the difficulty of binding reactants, hence reducing the overall catalytic efficiency. In contrast, the *cis*-to-*trans* isomerization can be catalyzed efficiently for most of those bonds because of negative ΔG_{cis} values. The lower ΔG_{cis} values are consistent with the general propensity for binding *cis* substrates more favorably than *trans* substrates for peptidyl-prolyl isomerases.[30] Only Pro151 and Pro152 have a negative or near-zero binding free energy for all states, and for both sites, the catalysis is mainly due to the creation of a more favored environment for the activated complex upon binding to CypD. The results collectively suggest that both Pro151 and Pro152 are potential binding

https://dx.doi.org/10.1021/acs.biochem.0c00946
Biochemistry 2021, 60, 597−606

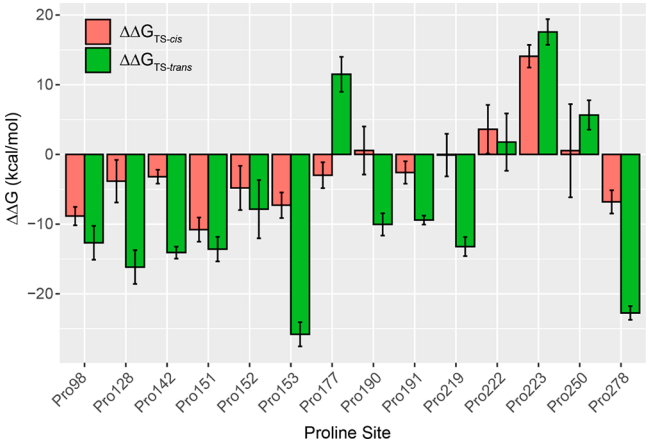

Figure 4. Relative binding free energies between the ground and transition states for all of the substrates derived from the p53 DNA binding domain. The binding free energy of a substrate in the TS conformation toward CypD is subtracted from that of the same substrate in either the *cis* or the *trans* conformation. The binding free energy difference, $\Delta\Delta G$, defines the reduction of the energy barrier during the *cis*−*trans* isomerization reaction. A more negative $\Delta\Delta G$ corresponds to a larger barrier reduction (due to a more stabilized CypD−p53 activated complex) and hence a higher turnover rate. The Pro151 substrate has the most balanced large barrier reduction during *cis*-to-*trans* and *trans*-to-*cis* transitions as both $\Delta\Delta G$ values are of similar highly negative values. Error bars represent the standard error of the mean (see Computational Methods).

sites for CypD, with Pro151 being more promising because of the larger activation energy reduction (more negative $\Delta\Delta G$).

In our binding free energy calculations, the configurational entropic cost (due to the loss of both external and internal degrees of freedom upon binding) was neglected. The same strategy was adopted in a recent docking and rescoring study using similar protocols.[58] The estimation of entropy has long been challenging, and in practice, whether including entropy will benefit or bring more errors into the calculation of binding free energy is controversial.[59,60] In our case, we followed the common assumption that the entropic impact is small especially for the relative binding free energy (i.e., between different substrates or isomerization conformations). Future studies may include a careful examination of the entropic effect using, for example, the cumulant expansion method developed by Minh and co-workers[61,62] and the more rigorous umbrella sampling and potential of mean force (PMF) calculations.

The selection of the optimal CypD binding site on p53 DBD cannot be determined by simply examining the local structural properties of all proline candidates. For CypD to bind, the targeted proline must be exposed to solvent, because otherwise side chains of neighboring residues would cause hindrance and reduce the accessibility of the catalytic site. We calculated the solvent-accessible surface area (SASA) for all 14 prolines in the p53 DBD to measure the magnitude of their solvent exposure. It shows that all of the prolines are exposed to solvent with various levels, except Pro278, which is completely buried in the protein interior (Table S2). This excludes the possibility of Pro278 being a CypD binding site, although the energetic analysis shows that the peptide bond preceding Pro278 is catalyzable. However, the optimal Pro151 displays an exposed area of only 11.5 Å^2 (<10% of the total area), smaller than all other exposed prolines. We argue that solvent exposure is a required condition for a proline to be the CypD binding site, but it alone cannot determine the precise location of the binding site, which is expected to be dynamic.

Isomerization at Pro151 Causes Local and Global Changes of Backbone Conformational Dynamics. The CypD binding site of the p53 DBD was identified on the basis of an inspection of the free energy barrier reduction along *cis*−*trans* isomerization, measured by relative binding free energies of the substrate in the transition state compared to the ground states. Previous experimental work showed that CypD binding and catalysis caused p53 to aggregate.[25] We assume that CypD binds the thermodynamically more stable *trans* conformation of Pro151 and catalyzes the isomerization into the *cis* form, leading to p53 aggregation, a process that was also linked to tumorigenesis.[63] To better understand this process, we examined the effect of prolyl bond isomerization at the predicted site (Pro151). Two additional MD simulations were performed for the full p53 DBD, each containing a distinct isomer state (*cis* or *trans*) at the peptide bond preceding Pro151. The apparent shift and alteration of the backbone conformational ensemble upon isomerization are observed (Figure 5A). The major conformational change separating the

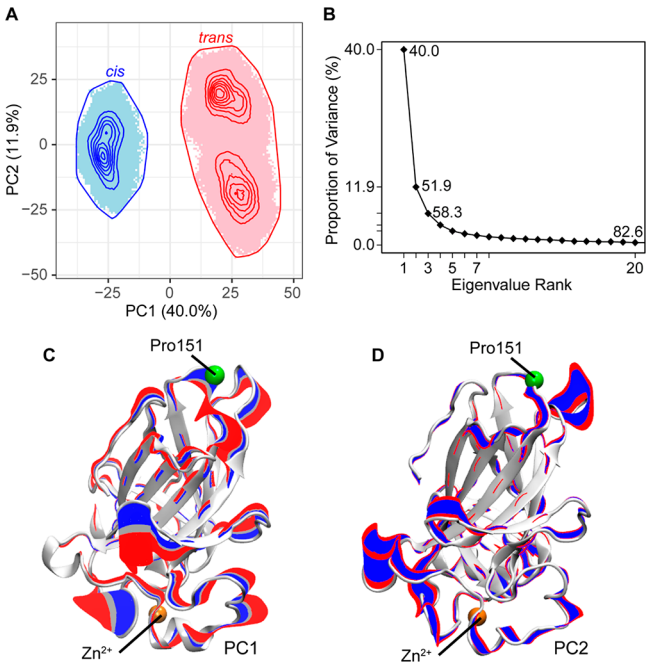

Figure 5. Principal component analysis (PCA) reveals local and global conformational changes of the p53 DNA binding domain upon *cis*−*trans* isomerization at Pro151. (A) Conformations of the p53 DNA binding domain generated from *cis*-Pro151 (blue) and *trans*-Pro151 (red) simulations are projected as shaded areas in the PC1−PC2 subspace (the number on the axis label indicates the percentage of variance captured by the corresponding PC). Contour lines represent probability density functions of conformations, and the outermost line indicates the boundary of sampled space. (B) Scree plot of the PCA showing the spectrum of eigenvalues. (C) Illustration of conformational changes captured by PC1 whose direction separates the two simulations. Blue, gray, and red lines indicate movements of corresponding regions along PC1 from *cis* to *trans* simulations, which occur at sites both close to and distal from Pro151, indicating an allosteric effect of the isomer switching. Proline 151 is shown as a green sphere, and the zinc ion (Zn^{2+}) is shown as an orange sphere. (D) Conformational changes captured by PC2, which do not separate *cis*-Pro151 and *trans*-Pro151 conformational ensembles.

https://dx.doi.org/10.1021/acs.biochem.0c00946
Biochemistry 2021, 60, 597−606

cis- and *trans*-p53 simulations, revealed by PC1 of the PCA applied to the simulation trajectories, occurs at both local residue sites close to Pro151 and distal loop regions near the DNA binding site where a zinc ion is bound (Figure 5C). Intriguingly, the two p53 systems also show distinct intrinsic dynamical properties as revealed by PC2: *trans* samples a broader conformational space, which contains two metastable substates, than *cis* (Figure 5A). The two substates of *trans* are separated mainly along PC2, which can be characterized by motions of loops both in the proximity of Pro151 and near the distal DNA binding region (Figure 5D). The more compact conformational ensemble of *cis* indicates that this system is overall more rigid, which might stabilize p53−p53 interactions and cause the aggregation of p53. Hence, we speculate that CypD binding catalyzes the isomerization of Pro151 from *trans* (which should be abundant in the absence of CypD) to *cis*, prompting p53 to aggregate. Note that PC1 and PC2 collectively capture more than half of the total structural variance of the simulations, with PC1 alone capturing 40% and both PC1 and PC2 capturing 51.9% (Figure 5B). This justifies our use of the two principal components to discuss dominant structural changes in the simulations.

To further understand the change in the internal conformational dynamics upon isomerization at Pro151, we calculated the residue-wise averaged atomic RMSF. Despite the overall similar pattern of RMSF, dramatic differences in residue flexibility between the simulations are observed at multiple regions, including Pro151 (Figure 6A). Except at Pro151, the

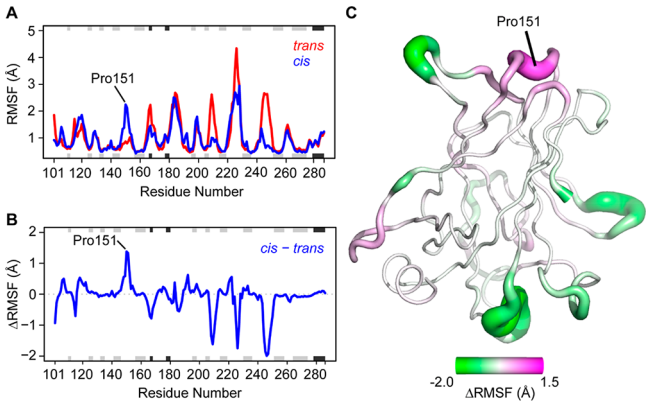

Figure 6. Backbone flexibility changes upon the isomerization at Pro151. (A) Residue-wise averaged backbone root-mean-square fluctuation (RMSF) calculated from *cis*-Pro151 (blue) and *trans*-Pro151 (red) simulations. A higher RMSF value indicates greater residue flexibility. Overall, *trans* is more flexible than *cis*, except for a region near Pro151 where an ∼1.5 Å larger RMSF in *cis* is observed. (B) Difference in RMSF (ΔRMSF) calculated by subtracting RMSF values of *cis* from those of *trans*. (C) Mapping of the ΔRMSF to the structure of the p53 DNA binding domain. Larger magnitudes of ΔRMSF are displayed by thicker tubes and darker green (negative) or magenta (positive) colors.

cis system is more rigid than the *trans* system (Figure 6B). This is consistent with the PCA result showing that the *cis* simulation samples much more compact conformational space [indicating an overall rigidity of the system upon isomerization from *trans* to *cis* (Figure 5A)]. The rigidification might make the *cis* system more prone to aggregation due to the smaller loss in conformational entropy. At Pro151, however, the *cis* form is more flexible. This indicates that upon isomerization from *trans* to *cis* at Pro151, local flexibility is enhanced to compensate the loss of entropy due to the reduction in global flexibility. Intriguingly, some of the rigidifications upon the *trans*-to-*cis* transition occur around the DNA binding surface (Figure 6C), correlating with the conformational change during the same transition revealed by PCA (Figure 5C). Clearly, these distal structural and dynamical changes represent an allosteric effect initiated at Pro151.

Residue−Residue Contact Analysis Reveals Allosteric Communication Pathways in the p53 DBD between Pro151 and Distal Sites. The isomerization at Pro151 causes both local and global structural and dynamical changes of the p53 DBD, indicating an allosteric communication between Pro151 and distal regions through the network of residue−residue interactions. To further understand the allosteric mechanism, we performed the difference contact network analysis (dCNA) that we developed recently.[57] In dCNA, conformational changes are characterized by variations of spatial distance between residues, quantified as residue−residue contact formation (coalescence) and breakage. The dCNA method was applied to compare conformational ensembles generated by the *cis*- and *trans*-p53 simulations; hence, the formation and breakage of contact discussed here are statistically meaningful (i.e., described by contact formation probability). The hypothesis is that the allosteric signal initiated at Pro151 can be relayed within the protein molecule by concerted contact probability changes that reflect both large-scale backbone/domain motions and subtle side-chain rearrangements. The result shows that significant contact changes (absolute probability difference of ≥0.1) from *trans* to *cis* occur all over the p53 DBD (Figure 7A). Large changes are mainly mediated by specific loops on the protein surface, connecting Pro151 to the DNA/Zn^{2+} binding site. Despite smaller magnitudes, contact changes are also observed in the protein interior, mediated by the central β sheets.

The dCNA community analysis was performed to better understand allosteric communication in the p53 DBD. A community consists of a group of residues; within a community, residues are more densely connected by invariant stable contacts, while between communities, the connections are looser (see ref 57 for more detail). Using communities, the description of protein structure and its associated conformational changes can be substantially simplified. A total of 12 communities are identified in the p53 DBD (Figure 7B). The four small communities on the flexible N- and C-termini are excluded from the subsequent analysis for the sake of clarity. For the eight remaining communities, collective contact changes from *trans* to *cis* between communities are summarized and depicted as a two-dimensional diagram in Figure 7C. In the community-level difference contact network, the overall change is contact formation (indicated by the predominant thick blue lines in Figure 7C). The largest change is the contact formation (with the sum of contact probability differences being 13.0) near the DNA/Zn^{2+} binding site (the yellow and white communities in Figure 7C), suggesting tightened interactions in the region. This explains the overall rigidity of *cis*-p53 observed in the PCA and RMSF analysis. Detailed inspections reveal a further split of the communities into two supergroups containing five (red, yellow, tan, light gray, and white circles in Figure 7C) and three communities (dark gray, green, and orange), respectively. The isomerization at Pro151 (in the dark gray community) causes contact

https://dx.doi.org/10.1021/acs.biochem.0c00946
Biochemistry 2021, 60, 597−606

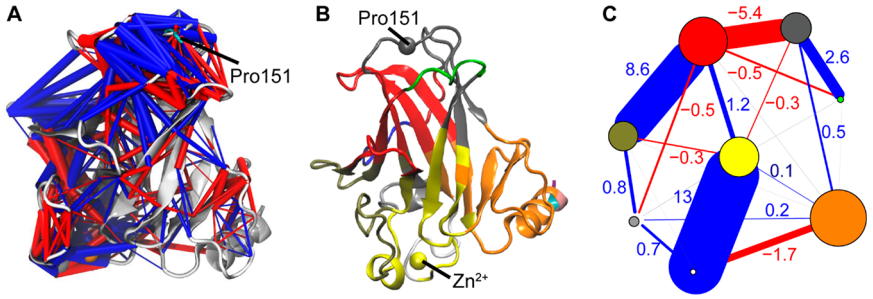

Figure 7. Difference contact network analysis (dCNA) reveals local and global contact rearrangements upon Pro151 isomerization. (A) Residue−residue contact probability changes (df) from *trans*-Pro151 to *cis*-Pro151 are mapped to the structure of the p53 DNA binding domain. Positive changes are represented as blue cylinders, and negative changes are represented as red cylinders, with cylinder radii proportional to $|df|$. Only significant contact changes (i.e., $|df| \geq 0.1$) are shown. (B) Detected residue communities are shown as colored regions of the cartoon. (C) Community difference network obtained by mapping the community partition obtained in panel B to the residue-wise difference network in panel A. Eight significant communities (excluding the four small communities at the flexible N- and C-terminal ends) are shown. Communities are represented by colored vertices (as in panel B), with the radius of vertex being proportional to the number of residues in the community. The line linking vertices describes the sum of contact probability changes ($\sum df$) between the communities. Blue (red) lines indicate positive (negative) net changes (with $\sum df$ labeled), and line widths are determined by $|\sum df|$.

breaking between the two supergroups (e.g., the local −5.4 net contact change between dark gray and red communities and the distal −1.7 net change between orange and white communities) while inducing overall contact formation within each supergroup. Hence, the dCNA community analysis provides insights into the structural basis for how the allosteric signal by Pro151 isomerization propagates in the residue contact network.

To gain insights into the residue-wise determinants of allosteric regulation in the p53 DNA binding domain, we examined significant ($|df| \geq 0.1$) contact changes between major communities. Three intercommunity regions were explored: the region between the dark gray and red communities around Pro151, between red and tan communities, and between yellow and white communities near the DNA binding site (see panels B and C of Figure 7 for the definition of community color). These regions show the largest overall community−community contact changes (Figure 7C). The largest individual contact changes between dark gray and red communities are around the triple-proline site, including Pro152−Thr155, Pro151−Tyr220, and Pro151−Thr155 (see Table S3 for the full list). All of these changes are dramatic contact breakages ($df < -0.98$), suggesting a strong local disruptive effect upon the isomerization. Major intercommunity contact changes near the DNA binding site are around Met246 from the white community, which forms stable contacts ($df > 0.97$) upon the isomerization with multiple residues from the yellow community, including Cys238, Leu194, and Asn239. Contact changes between red and tan communities are intriguing, because this region potentially mediates the allosteric communication between the triple-proline loop and the DNA binding site. In this region, the largest changes occur at Gln100 of the red community, which forms stable contacts ($df > 0.94$) with multiple residues from the tan community, including Thr211 and Asp208. Our results could be used to develop new small-molecule allosteric modulators of p53, which may target the identified key residues between red and tan communities, for example, and alter the conformational dynamics of the p53 DNA binding domain for modified activities.

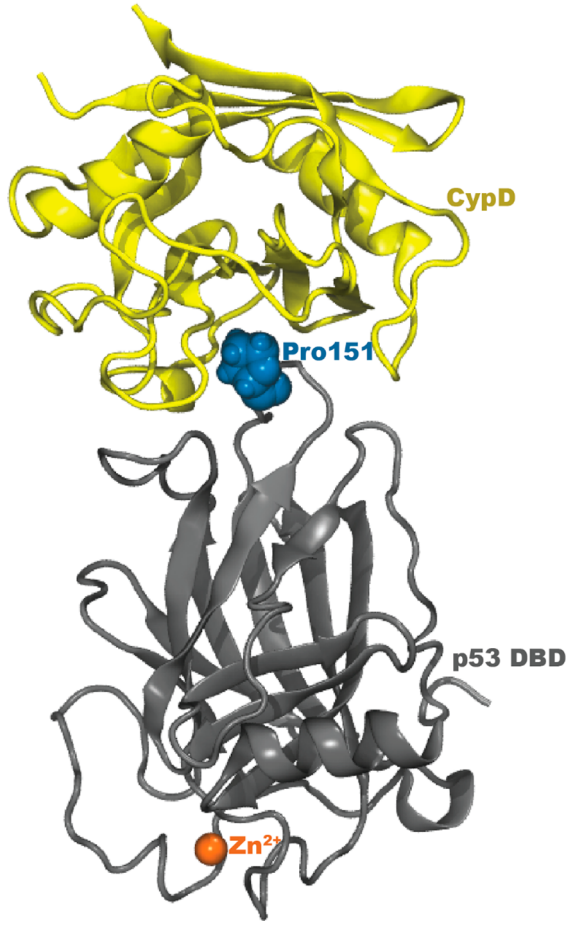

Figure 8. Structural model of p53 binding with CypD. The model represents the lowest binding free energy calculated from an MD simulation of the CypD−p53 complex. Proline 151 (in the *trans* conformation) of the p53 DBD is placed in the active site of CypD. The structure was rendered using VMD.

CONCLUSIONS

In this study, a comprehensive examination of the interaction between CypD and p53 truncated peptides was performed using MD simulations and associated MM/PBSA-based free energy calculations. Proline 151 on the triple-proline loop of

https://dx.doi.org/10.1021/acs.biochem.0c00946
Biochemistry 2021, 60, 597−606

the p53 DNA binding domain is predicted to be the site for p53 to bind CypD, a critical step during p53-mediated mitochondrial permeability transition pore opening and necrosis in response to oxidative stresses. Upon CypD binding, the *cis*−*trans* peptidyl-prolyl isomerization preceding Pro151 is catalyzed. We also characterized the effect of the isomerization at Pro151 and found that upon the transition from *trans* to *cis*, the overall p53 DBD becomes more rigid, which is compensated by an increase in local flexibility around Pro151. The dynamical changes induced by the isomerization occur in both local and distal regions, suggesting an allosteric effect. We delineated the potential allosteric communication pathways from Pro151 to distal sites, including the functional DNA binding surface. Our findings contribute to unveiling the mechanism underlying the formation of the CypD−p53 complex, which further help advance the understanding of the regulatory role of p53 in mitochondria. The result of scanning p53 peptides for catalyzable prolyl bonds may also be used in the development of potential isoform-specific inhibitors[64] for CypD, an important therapeutic target for the treatment of cancer.[63,65,66] For example, a potent inhibitor can be an artificial peptidomimetic that mimics the conformational state of a p53 peptide displaying a strong binding affinity for CypD (e.g., the transition state of Pro151 or the *trans* state of Pro223). To facilitate future studies, we provide a model of CypD−p53 complex structure (see Figure 8 and the Supporting Information for coordinates), which represents the lowest MM/PBSA binding free energy calculated from an additional CypD−p53 complex simulation.

■ ASSOCIATED CONTENT

Supporting Information

The Supporting Information is available free of charge at https://pubs.acs.org/doi/10.1021/acs.biochem.0c00946.

Probability distributions of the binding free energy between CypD and p53 peptides (Figure S1), probability distributions of the binding free energy between CypD and p53 peptides (Figure S2), protonation and tautomer states of histidine residues (Table S1), average and relative average binding free energies between the *cis* and *trans* forms toward the TS conformations for all proline sites in the p53 DNA binding domain (Table S2), and significant intercommunity contact changes in the p53 DNA binding domain upon Pro151 isomerization (*trans* to *cis*) (Table S3) (PDF)

Coordinates of the structural model of CypD-p53 DNA binding domain complex. (PDB)

■ AUTHOR INFORMATION

Corresponding Author

Donald Hamelberg − *Department of Chemistry and Center for Diagnostics and Therapeutics, Georgia State University, Atlanta, Georgia 30302-3965, United States;* orcid.org/0000-0002-3785-3037; Phone: (404) 413-5564; Email: dhamelberg@gsu.edu

Authors

Jacques Kumutima − *Department of Chemistry, Georgia State University, Atlanta, Georgia 30302-3965, United States*

Xin-Qiu Yao − *Department of Chemistry, Georgia State University, Atlanta, Georgia 30302-3965, United States;* orcid.org/0000-0003-2706-2028

Complete contact information is available at: https://pubs.acs.org/10.1021/acs.biochem.0c00946

Funding

This research was supported by the National Science Foundation (MCB - 2018144).

Notes

The authors declare no competing financial interest.

■ REFERENCES

(1) Levine, A. J. (1997) p53, the cellular gatekeeper for growth and division. *Cell 88*, 323−331.

(2) McLure, K. G., and Lee, P. W. (1998) How p53 binds DNA as a tetramer. *EMBO J. 17*, 3342−3350.

(3) Joerger, A. C., and Fersht, A. R. (2008) Structural biology of the tumor suppressor p53. *Annu. Rev. Biochem. 77*, 557−582.

(4) Olivier, M., Eeles, R., Hollstein, M., Khan, M. A., Harris, C. C., and Hainaut, P. (2002) The IARC TP53 database: new online mutation analysis and recommendations to users. *Hum. Mutat. 19*, 607−614.

(5) Pavletich, N. P., Chambers, K. A., and Pabo, C. O. (1993) The DNA-binding domain of p53 contains the four conserved regions and the major mutation hot spots. *Genes Dev. 7*, 2556−2564.

(6) Vaseva, A. V., Marchenko, N. D., Ji, K., Tsirka, S. E., Holzmann, S., and Moll, U. M. (2012) p53 opens the mitochondrial permeability transition pore to trigger necrosis. *Cell 149*, 1536−1548.

(7) Liu, D., and Xu, Y. (2011) p53, oxidative stress, and aging. *Antioxid. Redox Signaling 15*, 1669−1678.

(8) Krysko, O., Aaes, T. L., Kagan, V. E., D'Herde, K., Bachert, C., Leybaert, L., Vandenabeele, P., and Krysko, D. V. (2017) Necroptotic cell death in anti-cancer therapy. *Immunol. Rev. 280*, 207−219.

(9) Okada, Y., Numata, T., Sato-Numata, K., Sabirov, R. Z., Liu, H., Mori, S. I., and Morishima, S. (2019) Roles of volume-regulatory anion channels, VSOR and Maxi-Cl, in apoptosis, cisplatin resistance, necrosis, ischemic cell death, stroke and myocardial infarction. *Curr. Top. Membr. 83*, 205−283.

(10) Wang, P., and Heitman, J. (2005) The cyclophilins. *Genome Biology 6*, 226.

(11) Davis, T. L., Walker, J. R., Campagna-Slater, V., Finerty, P. J., Paramanathan, R., Bernstein, G., MacKenzie, F., Tempel, W., Ouyang, H., Lee, W. H., Eisenmesser, E. Z., and Dhe-Paganon, S. (2010) Structural and biochemical characterization of the human cyclophilin family of peptidyl-prolyl isomerases. *PLoS Biol. 8*, No. e1000439.

(12) Nath, P. R., and Isakov, N. (2015) Insights into peptidyl-prolyl cis-trans isomerase structure and function in immunocytes. *Immunol. Lett. 163*, 120−131.

(13) Galat, A. (2003) Peptidylprolyl cis/trans isomerases (immunophilins): biological diversity–targets–functions. *Curr. Top. Med. Chem. 3*, 1315−1347.

(14) Waldmeier, P. C., Zimmermann, K., Qian, T., Tintelnot-Blomley, M., and Lemasters, J. J. (2003) Cyclophilin D as a drug target. *Curr. Med. Chem. 10*, 1485−1506.

(15) Basso, E., Fante, L., Fowlkes, J., Petronilli, V., Forte, M. A., and Bernardi, P. (2005) Properties of the permeability transition pore in mitochondria devoid of Cyclophilin D. *J. Biol. Chem. 280*, 18558−18561.

(16) Porter, G. A., Jr., and Beutner, G. (2018) Cyclophilin D, Somehow a Master Regulator of Mitochondrial Function. *Biomolecules 8*, 176.

(17) Elrod, J. W., and Molkentin, J. D. (2013) Physiologic functions of cyclophilin D and the mitochondrial permeability transition pore. *Circ. J. 77*, 1111−1122.

(18) Elrod, J. W., Wong, R., Mishra, S., Vagnozzi, R. J., Sakthievel, B., Goonasekera, S. A., Karch, J., Gabel, S., Farber, J., Force, T., Heller

Brown, J., Murphy, E., and Molkentin, J. D. (2010) Cyclophilin D controls mitochondrial pore-dependent Ca(2+) exchange, metabolic flexibility, and propensity for heart failure in mice. *J. Clin. Invest. 120*, 3680−3687.
(19) Nakagawa, T., Shimizu, S., Watanabe, T., Yamaguchi, O., Otsu, K., Yamagata, H., Inohara, H., Kubo, T., and Tsujimoto, Y. (2005) Cyclophilin D-dependent mitochondrial permeability transition regulates some necrotic but not apoptotic cell death. *Nature 434*, 652−658.
(20) Lin, D. T., and Lechleiter, J. D. (2002) Mitochondrial targeted cyclophilin D protects cells from cell death by peptidyl prolyl isomerization. *J. Biol. Chem. 277*, 31134−31141.
(21) Bigi, A., Beltrami, E., Trinei, M., Stendardo, M., Pelicci, P. G., and Giorgio, M. (2016) Cyclophilin D counteracts P53-mediated growth arrest and promotes Ras tumorigenesis. *Oncogene 35*, 5132−5143.
(22) Du, H., Guo, L., Fang, F., Chen, D., Sosunov, A. A., McKhann, G. M., Yan, Y., Wang, C., Zhang, H., Molkentin, J. D., Gunn-Moore, F. J., Vonsattel, J. P., Arancio, O., Chen, J. X., and Yan, S. D. (2008) Cyclophilin D deficiency attenuates mitochondrial and neuronal perturbation and ameliorates learning and memory in Alzheimer's disease. *Nat. Med. 14*, 1097−1105.
(23) Martin, L. J., Semenkow, S., Hanaford, A., and Wong, M. (2014) Mitochondrial permeability transition pore regulates Parkinson's disease development in mutant α-synuclein transgenic mice. *Neurobiol. Aging 35*, 1132−1152.
(24) Halestrap, A. P., Kerr, P. M., Javadov, S., and Woodfield, K. Y. (1998) Elucidating the molecular mechanism of the permeability transition pore and its role in reperfusion injury of the heart. *Biochim. Biophys. Acta, Bioenerg. 1366*, 79−94.
(25) Lebedev, I., Nemajerova, A., Foda, Z. H., Kornaj, M., Tong, M., Moll, U. M., and Seeliger, M. A. (2016) A Novel In Vitro CypD-Mediated p53 Aggregation Assay Suggests a Model for Mitochondrial Permeability Transition by Chaperone Systems. *J. Mol. Biol. 428*, 4154−4167.
(26) Fayaz, S. M., and Rajanikant, G. K. (2015) Modelling the molecular mechanism of protein-protein interactions and their inhibition: CypD-p53 case study. *Mol. Diversity 19*, 931−943.
(27) Uchino, H., Elmér, E., Uchino, K., Li, P. A., He, Q. P., Smith, M. L., and Siesjö, B. K. (1998) Amelioration by cyclosporin A of brain damage in transient forebrain ischemia in the rat. *Brain Res. 812*, 216−226.
(28) Gijtenbeek, J. M., van den Bent, M. J., and Vecht, C. J. (1999) Cyclosporine neurotoxicity: a review. *J. Neurol. 246*, 339−346.
(29) Kim, S. J., Choi, H. K., and Lee, Y. B. (2002) Pharmacokinetic and pharmacodynamic evaluation of cyclosporin A O/W-emulsion in rats. *Int. J. Pharm. 249*, 149−156.
(30) Tork Ladani, S., Souffrant, M. G., Barman, A., and Hamelberg, D. (2015) Computational perspective and evaluation of plausible catalytic mechanisms of peptidyl-prolyl cis-trans isomerases. *Biochim. Biophys. Acta, Gen. Subj. 1850*, 1994−2004.
(31) Vöhringer-Martinez, E., and Dörner, C. (2016) Conformational Substrate Selection Contributes to the Enzymatic Catalytic Reaction Mechanism of Pin1. *J. Phys. Chem. B 120*, 12444−12453.
(32) Valasani, K. R., Carlson, E. A., Battaile, K. P., Bisson, A., Wang, C., Lovell, S., and Yan, S. (2014) High-resolution crystal structures of two crystal forms of human cyclophilin D in complex with PEG 400 molecules. *Acta Crystallogr., Sect. F: Struct. Biol. Commun. 70*, 717−722.
(33) Cho, Y., Gorina, S., Jeffrey, P. D., and Pavletich, N. P. (1994) Crystal structure of a p53 tumor suppressor-DNA complex: understanding tumorigenic mutations. *Science 265*, 346−355.
(34) Vu, P. J., Yao, X.-Q., Momin, M., and Hamelberg, D. (2018) Unraveling Allosteric Mechanisms of Enzymatic Catalysis with an Evolutionary Analysis of Residue-Residue Contact Dynamical Changes. *ACS Catal. 8*, 2375−2384.
(35) Case, D. A., Betz, R. M., Cerutti, D. S., Darden, T. A., Duke, R. E., Giese, T. J., Gohlke, H., Goetz, A. W., Homeyer, N., Izadi, S., Janowski, P., Kaus, J., Kovalenko, A., Lee, T. S., LeGrand, S., Li, P., Lin, C., Luchko, T., Luo, R., Madej, B., Mermelstein, D., Merz, K. M., Monard, G., Nguyen, H., Nguyen, H. T., Omelyan, I., Onufriev, A., Roe, D. R., Roitberg, A., Sagui, C., Simmerling, C. L., Botello-Smith, W. M., Swails, J., Walker, R. C., Wang, J., Wolf, R. M., Wu, X., Xiao, L., and Kollman, P. A. (2016) *AMBER 16*, University of California, San Francisco, San Francisco.
(36) Doshi, U., and Hamelberg, D. (2009) Reoptimization of the AMBER force field parameters for peptide bond (Omega) torsions using accelerated molecular dynamics. *J. Phys. Chem. B 113*, 16590−16595.
(37) Doshi, U., McGowan, L. C., Ladani, S. T., and Hamelberg, D. (2012) Resolving the complex role of enzyme conformational dynamics in catalytic function. *Proc. Natl. Acad. Sci. U. S. A. 109*, 5699−5704.
(38) Ladani, S. T., and Hamelberg, D. (2012) Entropic and Surprisingly Small Intramolecular Polarization Effects in the Mechanism of Cyclophilin A. *J. Phys. Chem. B 116*, 10771−10778.
(39) Tork Ladani, S., and Hamelberg, D. (2014) Intricacies of interactions, dynamics and solvent effects in enzyme catalysis: a computational perspective on cyclophilin A. *Mol. Simul. 40*, 765−776.
(40) Humphrey, W., Dalke, A., and Schulten, K. (1996) VMD: visual molecular dynamics. *J. Mol. Graphics 14*, 27−38.
(41) Maier, J. A., Martinez, C., Kasavajhala, K., Wickstrom, L., Hauser, K. E., and Simmerling, C. (2015) ff14SB: Improving the Accuracy of Protein Side Chain and Backbone Parameters from ff99SB. *J. Chem. Theory Comput. 11*, 3696−3713.
(42) Doshi, U., and Hamelberg, D. (2009) Reoptimization of the AMBER Force Field Parameters for Peptide Bond (Omega) Torsions Using Accelerated Molecular Dynamics. *J. Phys. Chem. B 113*, 16590−16595.
(43) Olsson, M. H., Søndergaard, C. R., Rostkowski, M., and Jensen, J. H. (2011) PROPKA3: Consistent Treatment of Internal and Surface Residues in Empirical pKa Predictions. *J. Chem. Theory Comput. 7*, 525−537.
(44) Mark, P., and Nilsson, L. (2001) Structure and Dynamics of the TIP3P, SPC, and SPC/E Water Models at 298 K. *J. Phys. Chem. A 105*, 9954−9960.
(45) Jorgensen, W. L. (1982) Revised TIPS for simulations of liquid water and aqueous solutions. *J. Chem. Phys. 77*, 4156−4163.
(46) Darden, T., York, D., and Pedersen, L. (1993) Particle mesh Ewald: An N·log(N) method for Ewald sums in large systems. *J. Chem. Phys. 98*, 10089−10092.
(47) Ryckaert, J.-P., Ciccotti, G., and Berendsen, H. (1977) Numerical-Integration of Cartesian Equations of Motion of a System with Constraints - Molecular-Dynamics of N-Alkanes. *J. Comput. Phys. 23*, 327−341.
(48) Kollman, P. A., Massova, I., Reyes, C., Kuhn, B., Huo, S., Chong, L., Lee, M., Lee, T., Duan, Y., Wang, W., Donini, O., Cieplak, P., Srinivasan, J., Case, D. A., and Cheatham, T. E. (2000) Calculating Structures and Free Energies of Complex Molecules: Combining Molecular Mechanics and Continuum Models. *Acc. Chem. Res. 33*, 889−897.
(49) Wickham, H. (2016) *ggplot2: Elegant Graphics for Data Analysis*, 2nd ed., Springer-Verlag, New York.
(50) Roe, D. R., and Cheatham, T. E. (2013) PTRAJ and CPPTRAJ: Software for Processing and Analysis of Molecular Dynamics Trajectory Data. *J. Chem. Theory Comput. 9*, 3084−3095.
(51) Grant, B. J., Rodrigues, A. P., ElSawy, K. M., McCammon, J. A., and Caves, L. S. (2006) Bio3d: an R package for the comparative analysis of protein structures. *Bioinformatics 22*, 2695−2696.
(52) Skjærven, L., Yao, X.-Q., Scarabelli, G., and Grant, B. J. (2014) Integrating protein structural dynamics and evolutionary analysis with Bio3D. *BMC Bioinf. 15*, 399.
(53) Barman, A., and Hamelberg, D. (2016) Coupled Dynamics and Entropic Contribution to the Allosteric Mechanism of Pin1. *J. Phys. Chem. B 120*, 8405−8415.
(54) Doshi, U., Holliday, M. J., Eisenmesser, E. Z., and Hamelberg, D. (2016) Dynamical network of residue-residue contacts reveals

https://dx.doi.org/10.1021/acs.biochem.0c00946
Biochemistry 2021, 60, 597−606

coupled allosteric effects in recognition, catalysis, and mutation. *Proc. Natl. Acad. Sci. U. S. A. 113*, 4735−4740.
(55) Sethi, A., Eargle, J., Black, A. A., and Luthey-Schulten, Z. (2009) Dynamical networks in tRNA:protein complexes. *Proc. Natl. Acad. Sci. U. S. A. 106*, 6620−6625.
(56) Yao, X.-Q., Momin, M., and Hamelberg, D. (2019) Establishing a Framework of Using Residue-Residue Interactions in Protein Difference Network Analysis. *J. Chem. Inf. Model. 59*, 3222−3228.
(57) Yao, X. Q., Momin, M., and Hamelberg, D. (2018) Elucidating Allosteric Communications in Proteins with Difference Contact Network Analysis. *J. Chem. Inf. Model. 58*, 1325−1330.
(58) Zhang, X., Perez-Sanchez, H., and Lightstone, F. C. (2017) A Comprehensive Docking and MM/GBSA Rescoring Study of Ligand Recognition upon Binding Antithrombin. *Curr. Top. Med. Chem. 17*, 1631−1639.
(59) Rastelli, G., Del Rio, A., Degliesposti, G., and Sgobba, M. (2010) Fast and accurate predictions of binding free energies using MM-PBSA and MM-GBSA. *J. Comput. Chem. 31*, 797−810.
(60) Greenidge, P. A., Kramer, C., Mozziconacci, J. C., and Wolf, R. M. (2013) MM/GBSA binding energy prediction on the PDBbind data set: successes, failures, and directions for further improvement. *J. Chem. Inf. Model. 53*, 201−209.
(61) Menzer, W. M., Li, C., Sun, W., Xie, B., and Minh, D. D. L. (2018) Simple Entropy Terms for End-Point Binding Free Energy Calculations. *J. Chem. Theory Comput. 14*, 6035−6049.
(62) Menzer, W. M., Xie, B., and Minh, D. D. L. (2020) On Restraints in End-Point Protein-Ligand Binding Free Energy Calculations. *J. Comput. Chem. 41*, 573−586.
(63) Kim, S., and An, S. S. (2016) Role of p53 isoforms and aggregations in cancer. *Medicine (Philadelphia, PA, U. S.) 95*, No. e3993.
(64) Sambasivarao, S. V., and Acevedo, O. (2011) Computational insight into small molecule inhibition of cyclophilins. *J. Chem. Inf. Model. 51*, 475−482.
(65) Lee, J., and Kim, S. S. (2010) Current implications of cyclophilins in human cancers. *J. Exp. Clin. Cancer Res. 29*, 97.
(66) Yao, Q., Li, M., Yang, H., Chai, H., Fisher, W., and Chen, C. (2005) Roles of cyclophilins in cancers and other organ systems. *World J. Surg. 29*, 276−280.

https://dx.doi.org/10.1021/acs.biochem.0c00946
Biochemistry 2021, 60, 597−606